International Journal of Extreme Manufacturing

Tool path generation and optimization for freeform surface diamond turning based on an independently controlled fast tool servo

OPEN ACCESS
IOP Publishing | IMMT
International Journal of Extreme Manufacturing
Int. J. Extrem. Manuf. 4 (2022) 025102 (16pp)
https://doi.org/10.1088/2631-7990/ac5f12

Tool path generation and optimization for freeform surface diamond turning based on an independently controlled fast tool servo

Yusuke Sato and Jiwang Yan*

Department of Mechanical Engineering, Keio University, Yokohama 223-8522, Japan

E-mail: yan@mech.keio.ac.jp

Received 4 December 2021, revised 11 January 2022
Accepted for publication 17 March 2022
Published 5 April 2022

Abstract

Diamond turning based on a fast tool servo (FTS) is widely used in freeform optics fabrication due to its high accuracy and machining efficiency. As a new trend, recently developed high-frequency and long-stroke FTS units are independently driven by a separate control system from the machine tool controller. However, the tool path generation strategy for the independently controlled FTS is far from complete. This study aims to establish methods for optimizing tool path for the independent control FTS to reduce form errors in a single step of machining. Different from the conventional integrated FTS control system, where control points are distributed in a spiral pattern, in this study, the tool path for the independent FTS controller is generated by the ring method and the mesh method, respectively. The machined surface profile is predicted by simulation and the parameters for the control point generation are optimized by minimizing the deviation between the predicted and the designed surfaces. To demonstrate the feasibility of the proposed tool path generation strategies, cutting tests of a two-dimensional sinewave and a micro-lens array were conducted and the results were compared. As a result, after tool path optimization, the peak-to-valley form error of the machined surface was reduced from 429 nm to 56 nm for the two-dimensional sinewave by using the ring method, and from 191 nm to 103 nm for the micro-lens array by using the mesh method, respectively.

Keywords: ultraprecision machining, diamond turning, fast tool servo, freeform surface, tool path optimization

1. Introduction

Freeform optics are non-axisymmetric optical elements with complex surface profiles. Due to their significant capabilities of adjusting light, freeform optics can improve optical performance and downsize optical systems, which gain popularity in the optical industry due to their high shape flexibility [1–3]. Therefore, freeform optics are widely employed in various optical products, such as camera systems, scanners, head-mounted displays, and components used in aerospace and biomedical engineering [4–6].

There are a wide variety of machining methods for freeform optics. Among them, ultra-precision diamond turning is superior in terms of surface quality and shape flexibility [7, 8]. In particular, it is possible to fabricate freeform surfaces with high efficiency by introducing fast tool servo (FTS) systems for ultra-precision diamond turning [9, 10].

* Author to whom any correspondence should be addressed.

2631-7990/22/025102+16$33.00

Conventionally, the FTS units are driven by piezoelectric actuators with the merits of fast response, high stiffness and motion resolution [11, 12]. However, due to their small strokes in micrometer scale, piezoelectric actuator-based FTS units are only used in limited applications. In recent years, long-stroke FTS units, equipped with voice coil driven air bearings, have been developed, which enable millimeter-level working strokes, and in turn, greatly expand the applications of FTS diamond turning. To improve the system compatibility and stability, most of the voice coil-based FTS units are independently driven by separate control systems from the main controllers of the machine tools [13]. Independently controlled FTS units are compatible with most of the commercial machine tools; thus, can be flexibly installed for variable applications in the industry. For these reasons, independently controlled FTS units have enormous potential to contribute to advanced freeform optics fabrication.

In tool path generation for the conventional FTS, the control points are laid out in a spiral pattern and the tool position is determined by linear interpolation using the adjacent control points [14, 15]. The deviation between the interpolated tool trajectory and the ideal tool path occurs, which leads to form errors on the surface profiles [16, 17]. Usually, adjacent control points are separated with a constant angle, namely the constant-angle method. The disadvantage of this method is that in the outer region, the distance between adjacent cutting points becomes larger; thus, the surface quality of the outer region is worse than that of the central region. To guarantee acceptable interpolation accuracy, a large number of control points with reduced angular separation is required, which leads to redundant control points for the region close to the rotation center. Facing this issue, some researchers attempted to reduce the form errors by adopting other strategies when laying out the control points on the tool path spiral. For example, Zhou *et al* [18] proposed the constant arc-length method, which successfully reduced the interpolation error by increasing the point cloud density in the outer region. However, the constant arc-length method leads to sparse control points placed in the inner region. In order to solve this issue, Neo *et al* [19] proposed a hybrid method which combines the constant angle method and the constant arc-length method. However, the above-mentioned strategies have no adaptation to surface shape variation, resulting in nonuniformity in surface quality. Zhu *et al* [16] proposed the adaptive tool servo, which takes the shape variation into the consideration. By this way, the interpolation error due to shape variation is remarkably reduced. Gong *et al* [20] proposed a tool path generation strategy based on space Archimedean spiral to fabricate the optical freeform surfaces of quasi-revolution. Besides the research of tool path generation strategy, a few previous works were focused on the interpolation method. The spline interpolation method is reported to be superior for generating smooth surfaces. However, the computation load of spline interpolation is several orders higher than that of general linear interpolation [17, 21].

On the other hand, for the independent FTS controller, the tool path program outputs the tool positions according to any arbitrary tool positions in the polar coordinate obtained from the machine tool. For this reason, the interpolation calculation based on the spiral tool path is not as efficient as on some more regular shapes, and the tool position is determined by two-dimensional interpolation adopting several nearby control points. Compared with the conventional FTS, the modeling and compensation of the interpolation error of an independently controlled FTS are much more complicated and under investigation, which is regarded as a bottleneck in FTS diamond turning of high-precision freeform surface generation. To the best of the authors' knowledge, little literature on the optimization or generation methods of tool path generation for independent controlled FTS units is available.

This study aims at proposing novel methods to optimize the tool path for the independent FTS control system to reduce form errors of machined surfaces caused by two-dimensional interpolation. The tool path is optimized by two steps to achieve the nanometer-level form accuracy. Firstly, control point clouds are pre-generated in two different methods, namely, ring method and mesh method. Based on the distribution of the control points, the final machined surface profile is predicted and interpolated by simulation. Then, by comparing the simulated surface with the designed surface, the form error is obtained. By repetitively adjusting the parameters of the control points, the form error was minimized to the desired tolerance. To demonstrate the feasibility of the proposed methods, cutting tests of two-dimensional sinewaves and micro-lens arrays were conducted on oxygen-free copper substrates under conditions with/without control point cloud optimization. The measurement results of the machined surface showed that after tool path optimization, the form error was significantly reduced for both the two-dimensional sinewaves and the micro-lens arrays.

2. Tool path generation

2.1. System control flow

Different from the conventional piezo-driven FTS units, voice coil-based FTS units are controlled by separate FTS controllers independent from the machine tool controllers. Figure 1 shows the control flow of an independently controlled FTS diamond turning system. In general, the hardware configuration involves three sections, including the controller of an *X*-*Z*-*C* three-axis machine tool, an FTS command generator and a proportional-integral-differential (PID) controller. In order to distinguish the motions of the machine tool and the FTS units in *Z* direction, the motion of FTS in *Z* direction is usually called *W*-axis motion. During diamond turning operations, the *X*-/*C*-axes positions are collected by grating encoders equipped in the machine tool and sent to the independent FTS controller as inputs of the FTS command generator. The command signal for the *W*-axis of the FTS unit corresponding to the *X*-/*C*-axes signals is generated by the FTS tool path program based on a specific algorithm. After that, the command signal for *W*-axis is amplified by the PID controller for driving the FTS unit.

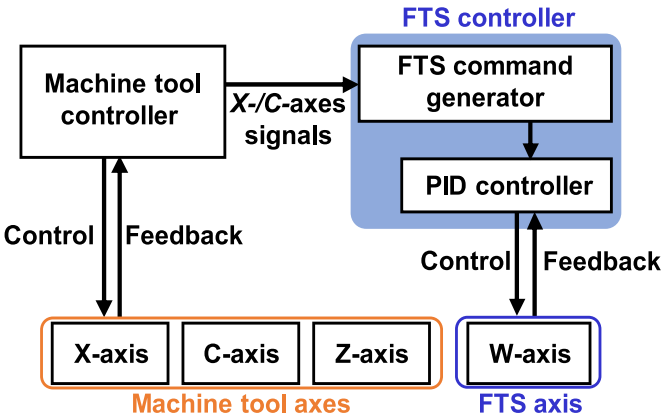

Figure 1. Control flow of an independently controlled FTS.

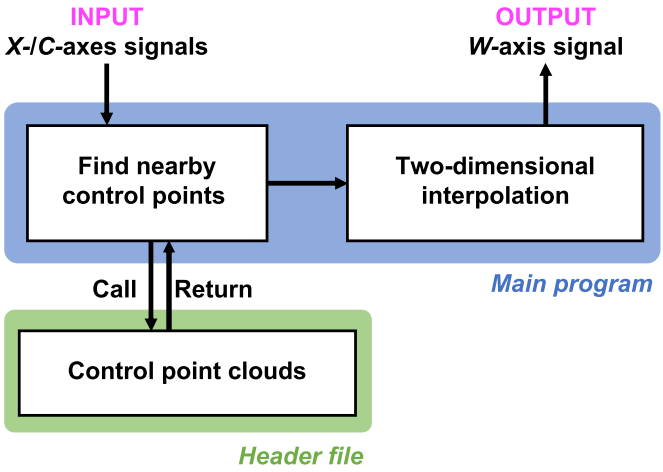

Figure 2. Overview of FTS tool path program.

2.2. Tool path program

For independently controlled FTS machining, the machine tool axes (X-/C-axes) and the FTS unit axis (W-axis) are synchronized to realize the desired motion coordinate. The machine tool axes (X-/C-axes) are controlled by the machine controller using a spiral tool path, whereas the FTS unit axis (W-axis) is motivated by the FTS controller using a separate FTS tool path which is not spiral. This means the two tool path programs independently operate in FTS machining. The spiral tool path and the FTS tool path realize different functions. In the program code of the spiral tool path, the control points are stored as a series of timeline-based commands, which are operated successively. In contrast, the FTS tool path program is not a timeline-based program but a real-time link function. The FTS tool path program receives the X-/C-axis signals, based on which, generates and outputs the corresponding W-axis signals instantly.

The details of the FTS tool path program are shown in figure 2. The program consists of a main program and a header file. The main program involves the data collection, two-dimensional interpolation and control signal generation, while the header file contains the whole control points, which are the tool coordinates of the W-axis in the polar coordinate of the machine tool. In order to obtain the tool positions by interpolation, in the FTS tool path program, the first step is to search for the nearby control points of the input X-/C-axes positions instantly. After that, the tool position is determined by two-dimensional interpolation using these nearby control points.

2.3. Layout of control point cloud

In order to instantly find the nearby control points in a two-dimensional coordinate system, the control point layout must be in the form of a two-dimensional grid. As shown in figure 3, the method of control point grid definition based on a polar coordinate is called the ring method, and the method of control point grid definition based on a Cartesian coordinate is called the mesh method. For the ring method, as shown in figure 3(a), the control points are placed on a series of concentric circles with a constant interval between them. On each circle, the

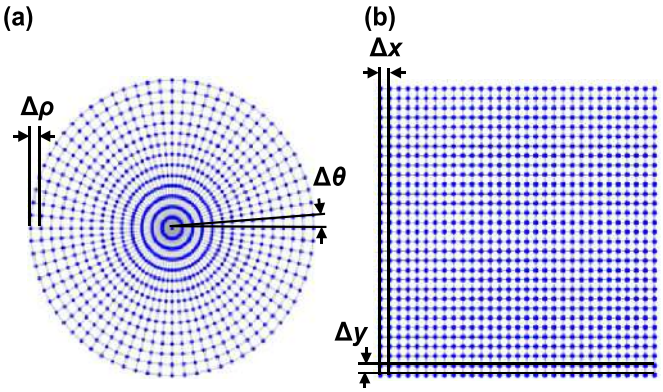

Figure 3. Layouts of control point clouds generated by (a) ring method (b) mesh method.

control points are uniformly distributed along the arc with a constant angle $\Delta\theta$. The pitch between adjacent concentric circles $\Delta\rho$ and the constant-angle $\Delta\theta$ are two key parameters in the tool path generation and optimization. The constant-angle $\Delta\theta$ is given as:

$$\Delta\theta = \frac{360}{N_p} \tag{1}$$

where N_p is the number of control points per revolution.

As shown in figure 3(b), the control point clouds generated by the mesh method forms a square pattern, where Δx and Δy are the intervals between two adjacent points in the X- and Y-axes.

Figure 4 shows the control point clouds for a freeform surface generated by the ring method and the mesh method. Control points generated by the ring method are represented in the polar coordinate (ρ, θ, w) and those generated by the mesh method are described in the Cartesian coordinate (x, y, w). The transition between the polar and the Cartesian coordinates is defined as follows:

$$x = \rho\cos(\theta) \tag{2}$$

$$y = \rho\sin(\theta) \tag{3}$$

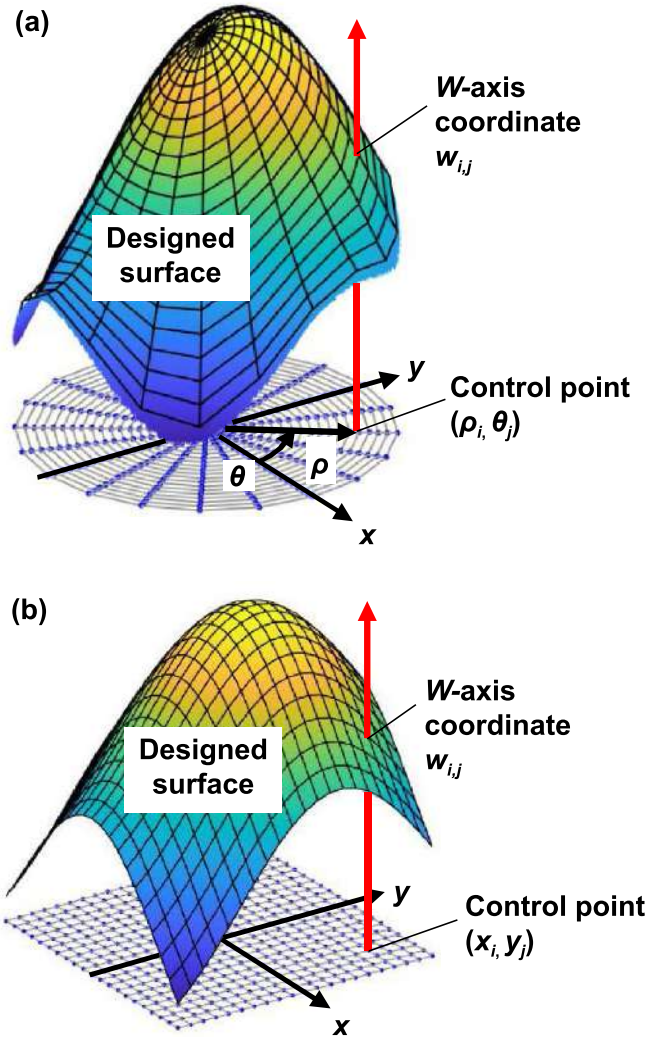

Figure 4. Schematics diagrams of point clouds generated by (a) ring method (b) mesh method.

$$w = f(x,y) = f(\rho\cos(\theta), \rho\sin(\theta)) \tag{4}$$

where f (•) describes the designed surface profile.

To demonstrate the proposed methods, a two-dimensional sinewave, which can be used as surface displacement sensors [22] etc, was used as the designed surface profile, as shown in figure 5(a). It can be mathematically described as follows:

$$f(x,y) = A_x \sin\left(\left(\frac{2\pi}{\lambda_x}\right)x + \phi_x\right) + A_y \sin\left(\left(\frac{2\pi}{\lambda_y}\right)y + \phi_y\right) \tag{5}$$

where A_x and A_y are amplitudes, and λ_x and λ_y are wavelength in x and y directions, respectively. In the demonstration, the parameters of the designed surface were set as $A_x = A_y = 0.5$ μm, $\lambda_x = \lambda_y = 100$ μm, $\phi_x = \phi_y = \pi/2$. The machining range was a circle with a radius of 1 mm.

As shown in figure 5(b), a micro-lens array, which can be used in Shack–Hartmann wavefront sensors [23, 24], etc, was also adopted as a designed surface profile. The profile of each lenslet was spherical. The f (•) of each lenslet is defined as follows:

$$f(x,y) = R - h - \sqrt{R^2 - (x-x_c)^2 - (y-y_c)^2} \tag{6}$$

where (x_c, y_c) is a center coordinate of each lenslet. R is a radius of lens curvature and h is a lens sag. In addition, a torus shape was inserted at the boundary between the plane and the micro-lens to smoothly blend them in three dimensions. The $f(\bullet)$ of a torus shape is defined as follows:

$$f(x,y) = \sqrt{r_t^2 - \left(\sqrt{(x-x_c)^2 + (y-y_c)^2} - R_t\right)^2} - \frac{r_t(R-h)}{R} \tag{7}$$

$$R_t = \sqrt{2hR - h^2}\left(1 + \frac{r_t}{R}\right) \tag{8}$$

$$r_t = \frac{R}{2} \tag{9}$$

where r_t is a radius of a tube and R_t is a distance from a center of a tube to a center of a torus. In the demonstration, the parameters of the micro-lens array were set as $R = 252.5$ μm and $h = 5$ μm. Each lenslet was placed on an orthogonal grid with a pitch of 0.15 mm. The whole micro-lens array machining range was within a square of 1.65 mm.

The control points are stored as a two-dimensional array $w_{m,n}$ in the C program. In the ring method, the first subscript m indicates the number of concentric circles and the second subscript n indicates the number of control points on each circle; whereas in the mesh method, the first subscript m and the second subscript n indicate the number of control points in X-axis and in Y-axis. Since the control points are stored in a two-dimensional array, the drawing range of the control point clouds becomes a circle in the ring method, and a rectangle in the mesh method, respectively. Therefore, in order to make effective usage of the control point clouds, it is better to use the ring method when the machining range layout of the free-form surface is circular, while use the mesh method when the layout is rectangular. In this study, the ring method was adopted for machining the two-dimensional sinewaves which have a circular layout and the mesh method for machining the micro lens array which has a rectangular layout.

2.4. Two-dimensional interpolation

In the tool path program, the tool position of the W-axis is determined by two-dimensional interpolation using nearby control points $w_{i,j}$. In this study, bilinear interpolation is adopted for two-dimensional interpolation [25]. The determination algorithm for tool positioning of W-axis using bilinear interpolation is shown in figure 6. Bilinear interpolation can be flexibly performed in a polar coordinate system for the

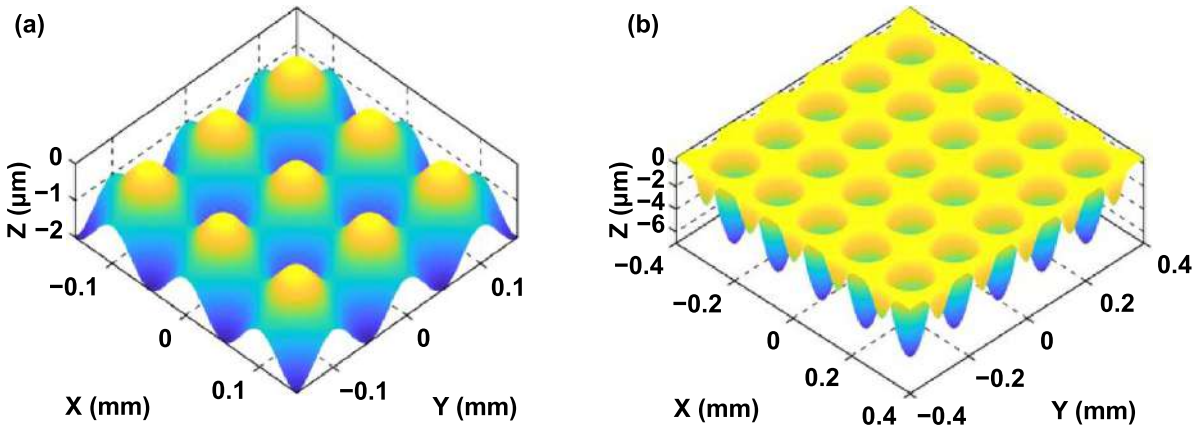

Figure 5. Schematic diagrams of designed surface profiles, (a) two-dimensional sinewave (b) micro-lens array.

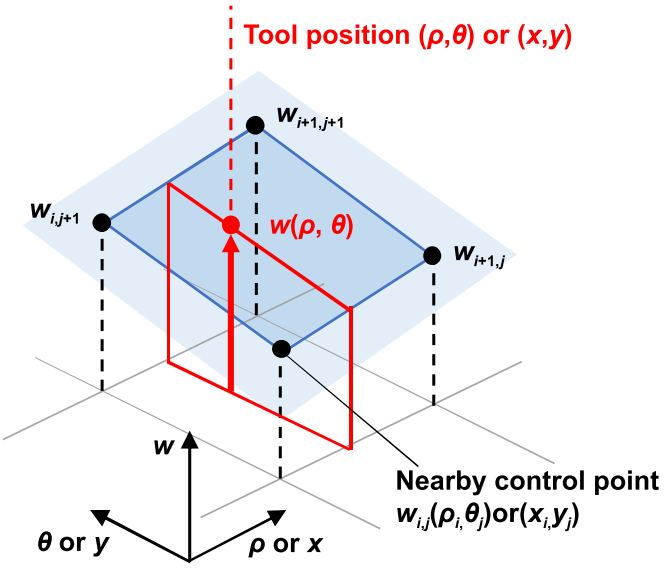

Figure 6. Determination of W-axis tool position using bilinear interpolation.

ring method, as well as in a Cartesian coordinate system for the mesh method. By bilinear interpolation based on the nearby control points, W-axis command tool position w can be expressed as follows:

$$w = (1-t)(1-u)w_{i,j} + t(1-u)w_{i+1,j} + tuw_{i+1,j+1} + (1-t)uw_{i,j+1}. \quad (10)$$

where, in the ring method, t, u are given as:

$$t = \frac{(\rho - \rho_i)}{(\rho_{i+1} - \rho_i)} \quad (11)$$

$$u = \frac{(\theta - \theta_j)}{(\theta_{j+1} - \theta_j)} \quad (12)$$

whereas, in the mesh method, t, u are given as:

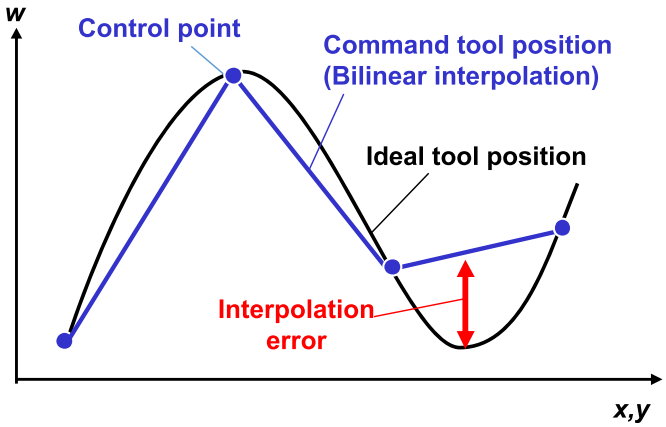

Figure 7. Schematic diagram of interpolation error formation.

$$t = \frac{(x - x_i)}{(x_{i+1} - x_i)} \quad (13)$$

$$u = \frac{(y - y_j)}{(y_{j+1} - y_j)} \quad (14)$$

where t and u cover a range between 0 and 1.

2.5. Interpolation error

After interpolation, the deviation between the ideal tool position and the actual command tool position cannot be completely eliminated, as shown in figure 7, which will introduce form errors on the final machined surface profile. Figure 8 shows a local area of predicted result of the interpolation error when tool path was generated using the ring method ($\Delta\rho = 2$ μm and $\Delta\theta = 2°$). It is clear that a deviation between the ideal tool path and the actual command tool position occurs due to the interpolation, which will affect the final machined surface profile and geometrical accuracy. Therefore, it is necessary to reduce the interpolation error within an acceptable range by optimizing the layout of the control points.

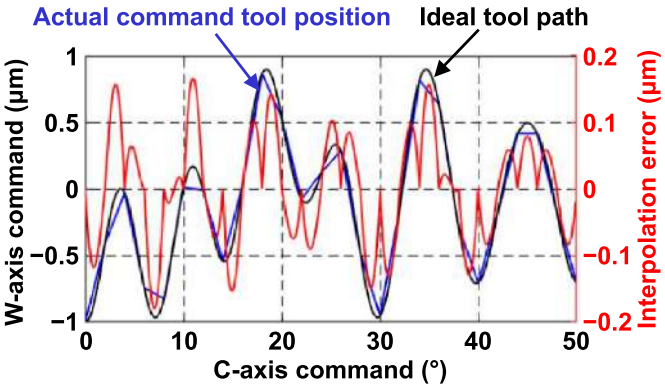

Figure 8. Predicted interpolation error for ring method ($\Delta\theta = 2°$, $\Delta\rho = 2$ μm).

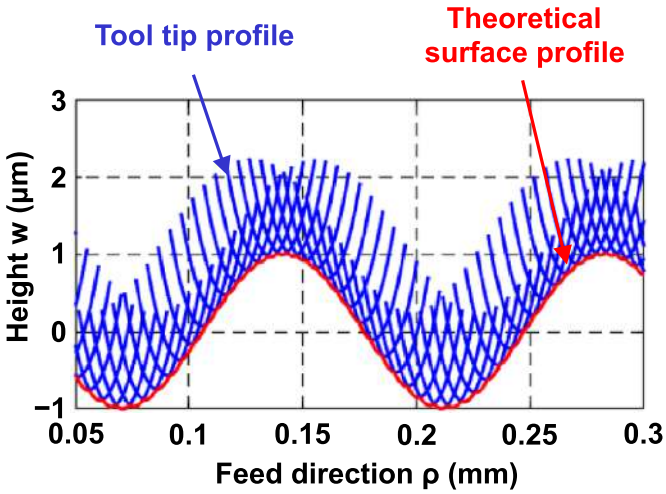

Figure 9. Example of theoretical surface profile along the feed direction.

3. Tool path optimization

3.1. Form error prediction

Prediction of final form error of workpiece was performed to optimize the layout of control points in FTS tool path program. In the form error prediction, the machined surface profile was predicted based on the simulation results of *W*-axis command tool positions. As shown in figure 9, the predicted final surface profile is described as the envelope of a continuous tool edge profile along the *W*-axis command tool positions in the feed direction [26, 27]. The tool edge profile in the feed direction can be expressed as follows:

$$z(\rho) = z_i + R_c - \sqrt{R_c^2 - (\rho - \rho_i)^2} \tag{15}$$

where R_c is the tool radius. ρ_i and z_i are the command tool positions in the polar coordinate. Then, the predicted surface profile z_{envelope} as the envelope of a continuous tool edge profile at radial position ρ can be calculated as the minimum value of all the tool edge profiles:

$$z_{\text{envelope}}(\rho) = \min\{z_k(\rho)\}. \tag{16}$$

After calculating the theoretical surface profile, the deviation between the predicted surface profile and the designed surface profile is achieved, which is treated as the final form error of the workpiece.

Figure 10 shows predicted results of the form error for the ring method when different parameters were adopted for the control points. Figures 10(a)–(c) show the results of form error prediction for three tool paths which have the different number of control points. The form error prediction was performed under the conditions that feed rate was 1 μm/rev, diamond tool radius was 0.083 mm, and machining area was a circle with a radius of 1 mm. In figure 10(a) where the number of control points was smallest among three tool paths (180 360 points), the form error was predicted to be 136 nm peak-to-valley (P-V) which was largest among the three cases. Then, with increasing the number of control points, such as figure 10(b) (360 720 points) and figure 10(c) (721 440 points), the form error decreased to 38 nm P-V and 12 nm P-V, respectively. In general, as the number of control points increases, the predicted form error becomes smaller due to the shrinkage of intervals between control points.

Further simulations were conducted to investigate the effects of geometrical parameters for the final form error. Figures 10(d)–(f) show the results of form error prediction with the same amount of control points over the same size of area but different sampling parameters. In figure 10(d) when the value of $\Delta\rho$ and $\Delta\theta$ were set as 0.38 μm and 1.000°, the predicted form error was 135 nm P-V. Figure 10(e) shows the results of the predicted form error when the value of $\Delta\rho$ was increased to 3.80 μm and $\Delta\theta$ was decreased to 0.100°, while the total number of control points was kept constant as the case in figure 10(d). The predicted form error in figure 10(e) (10 nm P-V) was much smaller than that in figure 10(d). Moreover, with a further incensement of $\Delta\rho$ (12.20 μm) and a decrease of $\Delta\theta$ (0.031°), the predicted form error result, as shown in figure 10(f) (75 nm P-V) was larger than that in figure 10(e) (10 nm P-V). These results showed that even if the number of control points was the same, if the ratio of $\Delta\rho$ and $\Delta\theta$ was not appropriate, interpolation error occurred and eventually led to the form error in the final machined surface. Therefore, the ratio of $\Delta\rho$ to $\Delta\theta$ should be optimized and was defined as the aspect ratio given as follows:

$$\alpha_{\text{ring}} = \frac{\Delta\rho\,(\mu\text{m})}{\Delta\theta\,(\text{deg})}. \tag{17}$$

Introducing the aspect ratio α_{ring} enables to quantitatively describe the effect of these two parameters when the number of control points of the tool path is the same. Besides, the distribution pattern of the interpolation error highly depends on the aspect ratio, and it is also considered that there is an optimal aspect ratio that can remarkably minimize the interpolation error.

More numerical predictions were done to investigate the connections between the ratio and the form error. The aspect ratios α_{ring} in figures 10(d)–(f) were set as 0.379, 38.0 and 390 and the number of control points was kept constant in these

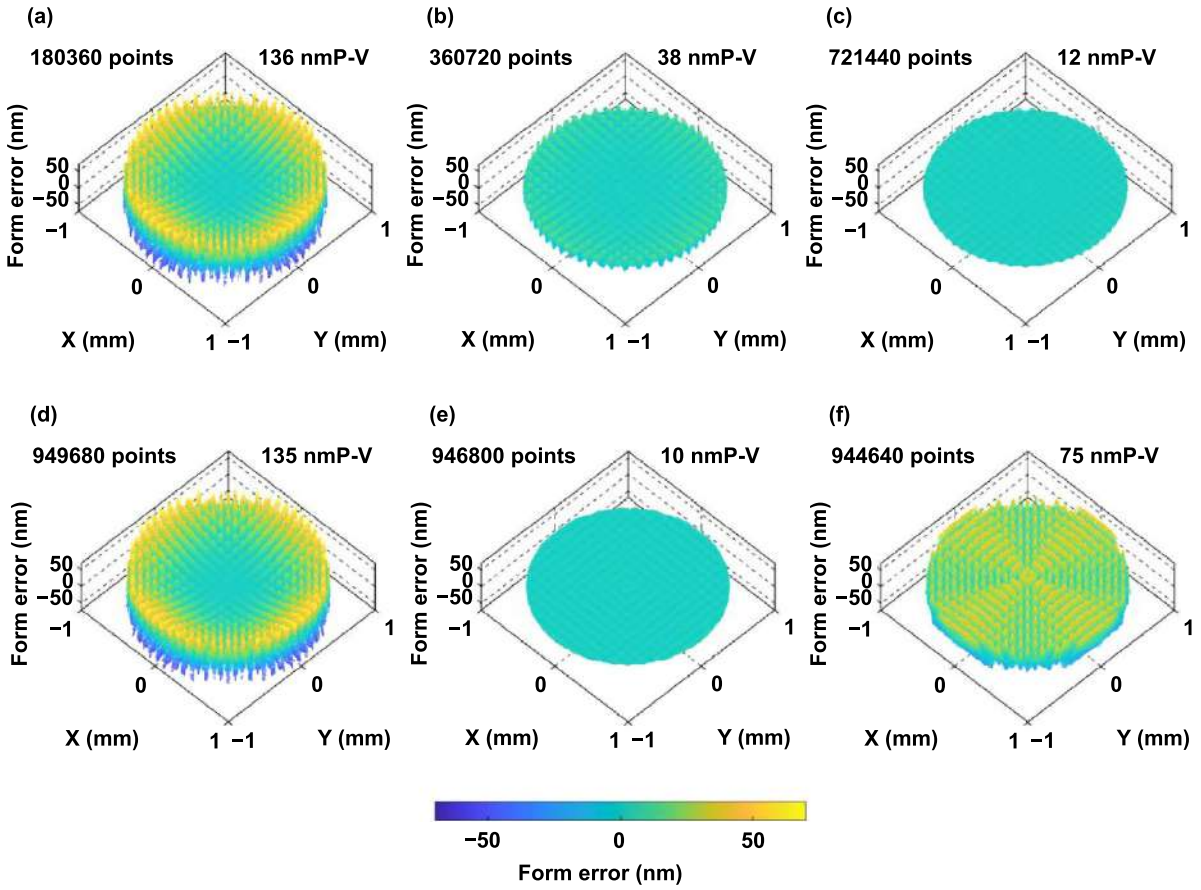

Figure 10. Predicted form error with ring method: (a) $\Delta\rho = 2.00$ μm, $\Delta\theta = 1.000°$, (b) $\Delta\rho = 2.00$ μm, $\Delta\theta = 0.500°$, (c) $\Delta\rho = 2.00$ μm, $\Delta\theta = 0.250°$, (d) $\Delta\rho = 0.38$ μm, $\Delta\theta = 1.000°$, (e) $\Delta\rho = 3.80$ μm, $\Delta\theta = 0.100°$, (f) $\Delta\rho = 12.20$ μm, $\Delta\theta = 0.031°$.

cases. Since the form error in figure 10(e) was the smallest, it was thought that the optimal aspect ratio was supposed to be around 38.0. The aspect ratio of figure 10(d) was smaller than the optimal aspect ratio, in other words, $\Delta\theta$ was relatively larger compared to $\Delta\rho$, leading to large interpolation error. This might be because in the outer region, the distance between two adjacent control points in the circumferential direction was larger caused by large $\Delta\theta$. On the other hand, the aspect ratio of figure 10(f) was larger than the optimal aspect ratio, in which the $\Delta\rho$ was relatively large compared to $\Delta\theta$, also leading to large interpolation error. This might be due to the large distance between two adjacent control points in the radial direction caused by large $\Delta\rho$. In addition, comparing the predicted form error distributions in figures 10(d) and (f), it was observed in figure 10(d) that the form error was much larger on the outer region of the machined surface, while in figure 10(f), the form errors on the inner and outer regions of the machined surface are almost the same. This indicated that the aspect ratio had a significant influence on the uniformity of form error distribution.

The form error prediction was also performed for a micro-lens array. The whole dimension of the machined micro-lens array was set to a 1.65×1.65 mm^2 square. The form error prediction was performed under the conditions that feed rate was 1 μm/rev and diamond tool radius was 0.083 mm. Figure 11 shows the prediction result of form errors when the mesh method was adopted. The results of form error with the different number of control points are shown in figure 11(a) (43 681 points), (b) (172 225 points) and (c) (683 929 points). The form error in figure 11(c) is 16 nm P-V, which was smaller than that in figure 11(a) (164 nm P-V) and figure 11(b) (42 nm P-V). Similarly to the two-dimensional sinewave surface with the ring method, as the number of control points increased, the predicted form error became smaller. In the mesh method, the ratio of Δx to Δy was also defined as the aspect ratio given as:

$$\alpha_{\text{mesh}} = \frac{\Delta x\,(\mu\text{m})}{\Delta y\,(\mu\text{m})}. \tag{18}$$

Figures 11(d)–(f) show the results of form error with three tool paths with different aspect ratio, while both of the number of points were almost the same. As shown in figure 11(e), when the aspect ratio was 1.00, the form error (14 nm P-V) was the smallest among three results. When the aspect ratio became larger in figure 11(d) ($\alpha_{\text{mesh}} = 8.78$) or smaller in figure 11(f) ($\alpha_{\text{mesh}} = 0.0810$) than that, the form error became larger, 48 nm P-V and 66 nm P-V, respectively. It is also necessary to search for the optimal aspect ratio for the mesh method. For all results in figure 11, the form error was predicted to be uniformly distributed over the entire machined surface. One possible reason is that the control point pitch Δx, Δy is constant regardless of location in the mesh method. The interpolation

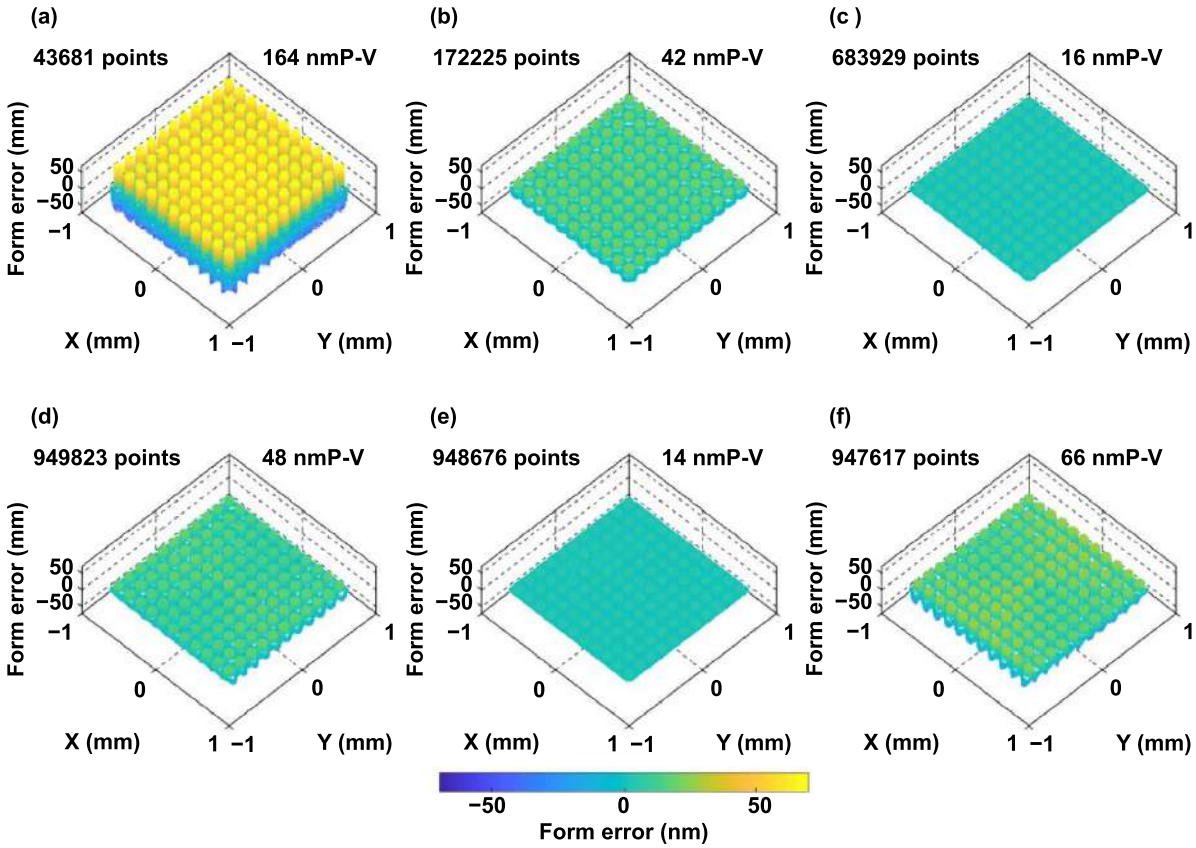

Figure 11. Predicted form error with mesh method: (a) Δx, $\Delta y = 8.00$ μm, (b) Δx, $\Delta y = 4.00$ μm, (c) Δx, $\Delta y = 2.00$ μm, (d) $\Delta x = 5.02$ μm, $\Delta y = 0.57$ μm, (e) Δx, $\Delta y = 1.69$ μm, (f) $\Delta x = 0.48$ μm, $\Delta y = 5.96$ μm.

form error was different from the pattern occurred in the ring method.

3.2. Optimization of control points layout

Based on the aforementioned prediction results, it is necessary to abstract the key effects of each factor in form error, such as the number of control points and aspect ratio. Figure 12(a) shows the relation between the number of control points and the P-V value of the predicted form error, where the aspect ratio was constant along each curve. From the results, it was found that the larger number of control points was utilized, the smaller the prediction form error became. Thus, in order to achieve high accuracy, it is preferable to have as many control points as possible for tool path generation. However, an FTS controller has a limited volume to store the control points and too many control points would reduce the processing speed. Therefore, it is also necessary to optimize the capability of each control point with an effective layout by considering the effect of the aspect ratio. Figure 12(b) shows the relation between the aspect ratio α_{ring} and the corresponding predicted form error with similar number of control points (950 000 points). From the result, it was notable that the relation between the ratio and the predicted form error was not linear. The predicted form error (8 nm P-V) was the smallest when aspect ratio α_{ring} was 24.3 ($\Delta\rho = 3.04$ μm, $\Delta\theta = 0.125°$), which should be considered as the optimal geometrical parameters for the selected surface profile.

Similarly to the two-dimensional sinewave surface with the ring method, the tool path optimization was performed for micro-lens array machining with the mesh method. Figure 13(a) shows the relation between the number of control points and the P-V value of the predicted form error, where the aspect ratio was constant along each curve. As the same as ring method, the larger the number of point clouds was, the smaller the prediction form error became. Figure 13(b) shows the relation between the aspect ratio α_{mesh} and the predicted form error with fixed number of control points (950 000 points). The predicted form error (14 nm P-V) was the smallest when aspect ratio α_{mesh} was 1.0 ($\Delta x = 1.69$ μm, $\Delta y = 1.69$ mm). Consequently, the optimal layout parameters of the mesh method were detected.

In this study, as examples, tool path optimization was performed for two-dimensional sinewaves and a micro-lens array. As the optimal layout parameters depend on the designed surface, to help the optimization of tool path for different designed surfaces, a flowchart of tool path optimization based on the ring and mesh methods is presented in figure 14. After a freeform surface is designed, the machining conditions, such as machining range, feed rate, and the radius of the diamond tool, are selected. Then, an FTS tool path is generated based on the layout parameters of the control points, i.e. the number of control points and aspect ratio. Finally, form error prediction

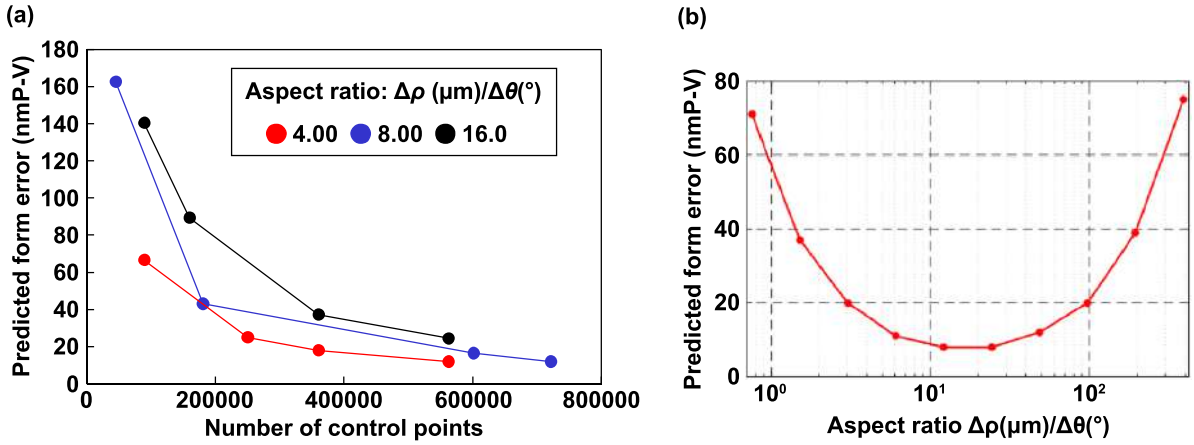

Figure 12. Relation between predicted form error and (a) number of control points (b) aspect ratio, for two-dimensional sinewave with ring method.

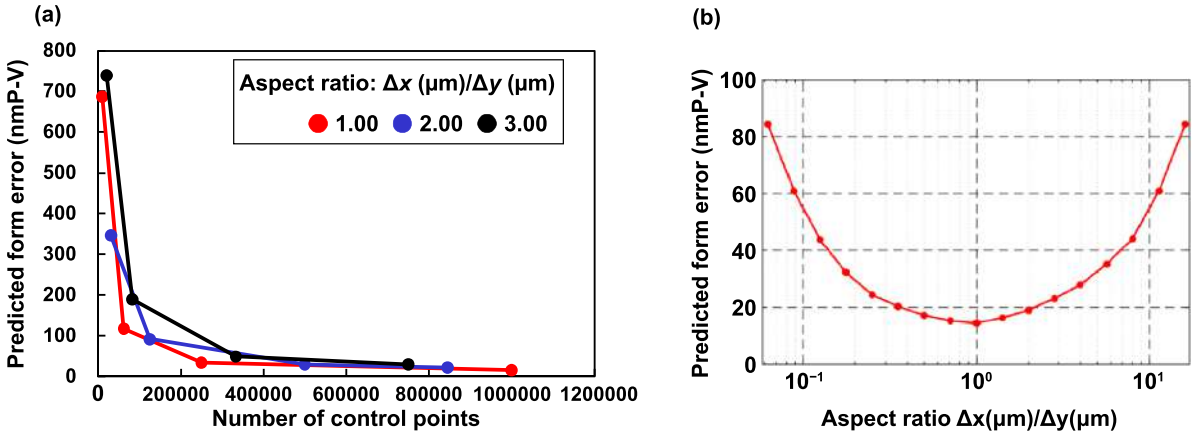

Figure 13. Relation between predicted form error and (a) number of control points (b) aspect ratio, for micro-lens array with mesh method.

is performed, and if the P-V value of the predicted form error is smaller than the tolerance, the tool path is used for machining. If the predicted form error exceeds the tolerance, the layout parameters are redefined, and tool path generation and form error prediction are performed again.

4. Experimental validation

4.1. Experimental procedure

To verify the feasibility of the optimization methods for tool path, a two-dimensional sinewave and a micro-lens array were test-fabricated on oxygen-free copper. An ultra-precision lathe, Nanoform X (AMETEK Precitech Inc., US), and a FTS unit, FTS-5000 (AMETEK Precitech Inc., US), were used in the experiment, as shown in figure 15. Table 1 shows the typical performance of FTS-5000 [13]. A single-crystal diamond tool (K&Y Diamond Ltd, Canada) with a nose radius of 0.083 mm, a rake angle of 0° and a clearance angle of 14° was used. The two-dimensional sinewave and the micro-lens arrays were machined under the same cutting conditions shown in table 2. In this experiment, three tool path programs were generated for each kind of surface structure. Two of them were without optimization (case 1 and 2) and the third was based on the optimal parameters obtained from the aforementioned prediction (case 3). For the tool path of case 1, the number of control points was much smaller than the limit of FTS-5000 (∼one million). For that of case 2, the number of control points reached the limit of FTS-5000 but the aspect ratio was not optimized. As these three cases cover most of the conditions in the practical tool path generation, by comparing these cases, the feasibility and the effectiveness of the proposed method can be confirmed. Table 3 presents the detailed parameters for tool path generation. The ring method was selected for two-dimensional sinewave fabrication and the mesh method for micro-lens array fabrication, respectively. The command rate of FTS-5000 is 20 kHz, as shown in table 1, while the spindle rotation speed in the verification experiments was 50 rpm during the finishing cut, as shown in table 2. This means that 24 000 signals are sent to the FTS controller per spindle revolution. On the other hand, as an example, the number of control points per revolution of the optimized tool path (case 3) by the ring method is 2880 points, which is much less than 24 000. Therefore, the FTS controller and the interpolation program have adequate capability to process the data and output the corresponding positions, and

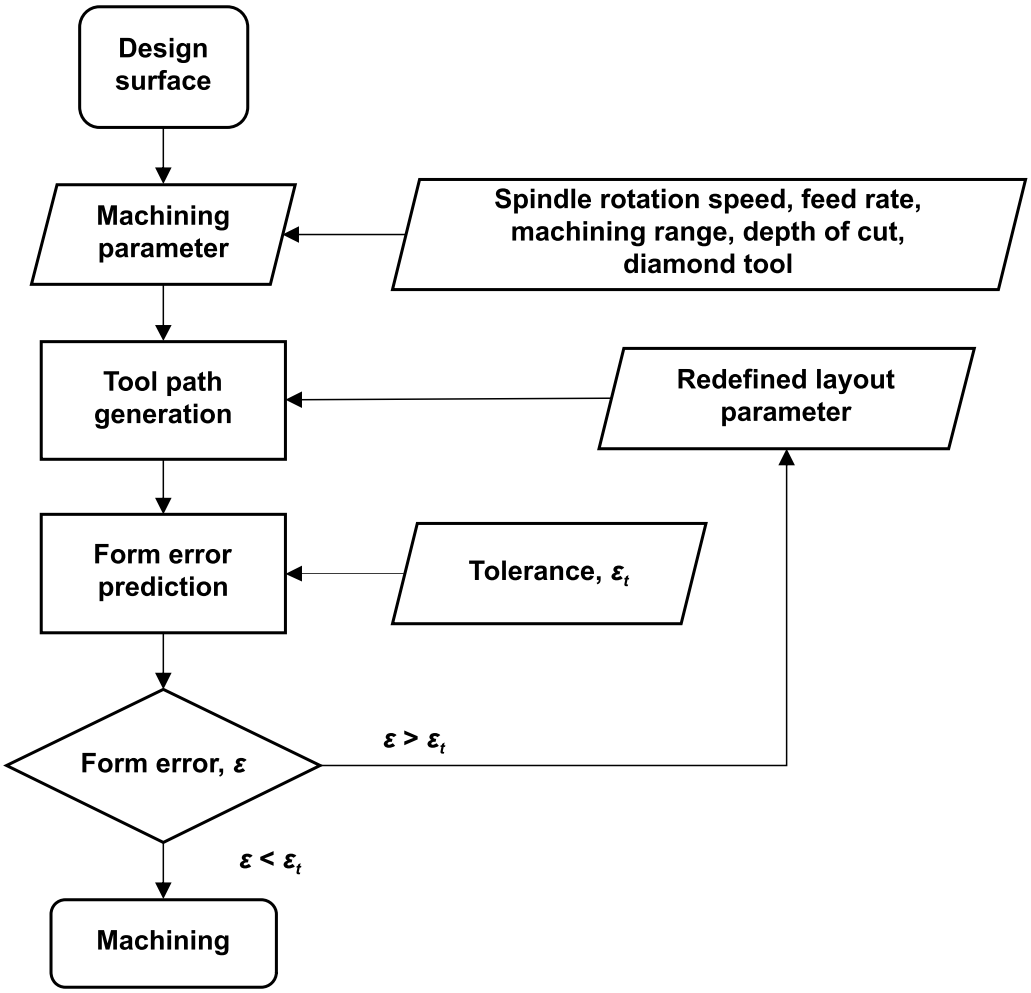

Figure 14. Flowchart of tool path optimization procedure.

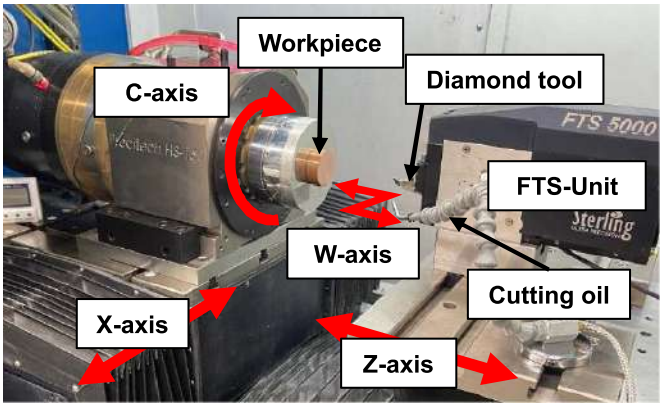

Figure 15. Photograph of the set-up of FTS diamond turning.

thus the command rate does not affect the determination of the control point clouds layout. Before machining, the frequency spectrum of W-axis motion trajectory was estimated from the generated tool path and spindle rotation speed as shown in figure 16. To prevent the occurrence of dynamic errors, the maximum frequency of the W-axis motion trajectory must be less than the closed-loop bandwidth of the FTS [27]. From the predicted results shown in figures 16(a) and (b), the maximum frequencies of both the spectrums of the two-dimensional sinewave and the micro-lens array are much smaller than the typical operational sinusoidal acceleration (440 Hz at an amplitude of 100 μm) of FTS-5000. Therefore, under the present conditions, stable tool motion can be achieved.

Table 1. Typical performance of FTS-5000.

Typical performance	Values
Peak acceleration (m s^{-2})	400
Continuous acceleration (m s^{-2})	250
Travel (μm)	5000
Typical operational sinusoidal acceleration at amplitude of 100 μm (Hz)	440
Command rate (kHz)	20

Table 2. Cutting conditions.

Cutting parameters	Values
Depth of cut (μm)	5 (Rough cut) 1 (Finish cut)
Spindle rotation rate N (rpm)	100 (Rough cut) 50 (Finish cut)
Feed per revolution f (μm/rev)	5 (Rough cut) 1 (Finish cut)
Cutting tool	
Tool material	Single-crystal diamond
Nose radius (mm)	0.083
Rake angle (°)	0
Clearance angle (°)	14
Coolant	Oil mist

Table 3. Detailed parameters for FTS tool path program.

For two-dimensional sinewave					
	Layout	Aspect ratio	$\Delta\rho$ (μm)	$\Delta\theta$ (°)	Number of points
Case 1:	Ring	1.00	2.00	2.00	90 180
Case 2:	Ring	0.38	0.38	1.00	949 680
Case 3:	Ring	24.3	3.04	0.125	947 520
For micro-lens array					
	Layout	Aspect ratio	Δx (μm)	Δy (μm)	Number of points
Case 1:	Mesh	1.00	8.00	8.00	43 681
Case 2:	Mesh	16.1	6.79	0.424	946 485
Case 3:	Mesh	1.00	1.69	1.69	948 676

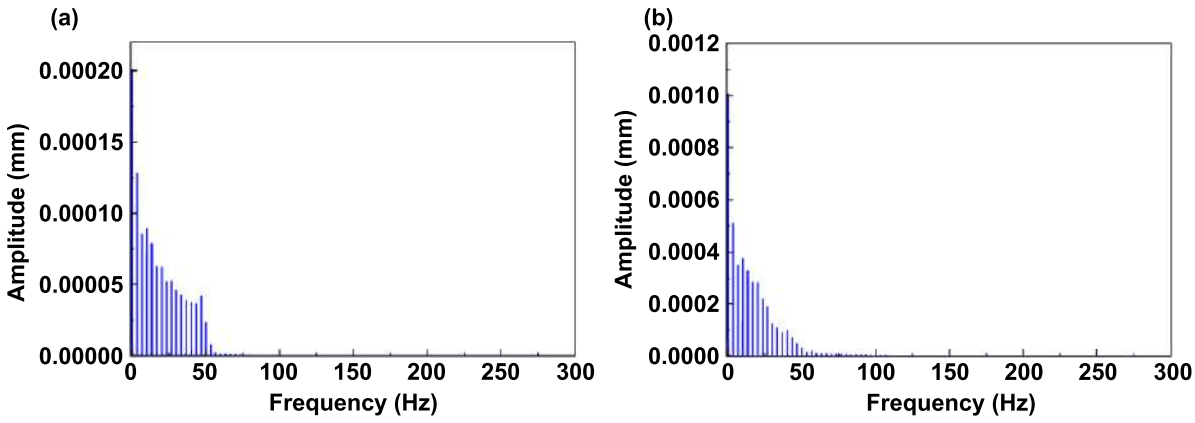

Figure 16. Frequency spectrum of W-axis motion trajectory for: (a) two-dimensional sinewave (b) micro-lens array, with 50 rpm and FTS tool path program case 3.

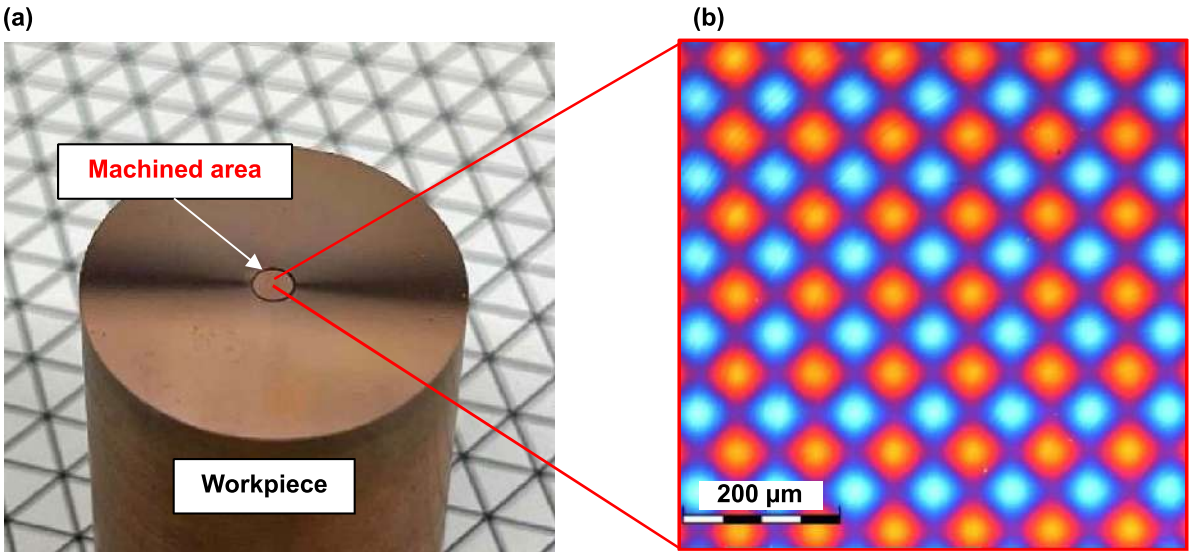

Figure 17. Photograph of a machined two-dimensional sinewave on oxygen-free copper workpiece: (a) optical image, (b) differential interference contrast microscope image.

After machining, the surface was cleaned with acetone to remove the attached chips then observed and measured by a white light interferometer Nexview N2 (AMETEK Zygo Corp., US) and a laser microscope OLS4100 (Olympus Corp., Japan).

4.2. Results and discussion

Figure 17(a) is a photograph of a machined workpiece of two-dimensional sinewaves. Figure 17(b) shows a microscope image of the two-dimensional sinewave machined with the optimized tool path parameter, indicating that a smooth surface was obtained. Figure 18 shows micro-topographies and the residual form error of the machined surface. Figure 18(a) shows the residual form error of case 1 where the tool path was set to a coarse control point cloud (90 180 points). The residual form error was 429 nm P-V, which was the largest among case 1, 2 and 3. It can be observed that form error was distributed in a wave pattern along the cutting direction. Figures 18(b) and (c) show the residual form error of case 2 and 3 with the number of control points close to one million. In figure 18(c), no form error of the wave pattern was observed, which is different from figure 18(b). Moreover, it was observed that the residual form error (56 nm P-V) in figure 18(c) was much smaller than that in figure 18(b) (236 nm P-V), because the aspect ratio of tool path in figure 18(c) was optimized. Among these three results, the form error was the smallest when the optimized tool path was adopted, demonstrating the feasibility of the proposed optimization method for the ring method.

Figure 19 shows a microscope image of a micro lens array machined with an optimized tool path parameter (mesh method: $\Delta x = 1.69$ μm and $\Delta y = 1.69$ μm). All lenslets shared the same feature with no structure and position distortions, suggesting that uniform quality of the micro-lens array covering a large area was precisely machined. Figure 20 shows the micro-topographies and residual form error on the selected lenslet marked out in the red square in figure 19. In figure 20(a), the residual form error was 191 nm P-V when the tool path was set to a coarse control point cloud (43 681 points). It was observed that the form error was symmetrically distributed in the X and Y directions. Figures 20(b) and (c) show the machined results when the number of control points was set to almost the maximum. In figure 20(b) with an inappropriate aspect ratio, it was observed that form error depending on the x-axis direction occurred in figure 20(b). One possible reason is that the resolution of x-axis direction was lower than the resolution of y-axis direction due to that the set value of Δx is larger than Δy. On the other hand, the residual form error (103 nm P-V) of figure 20(c) was smaller than that of figure 20(a) (191 nm P-V) and figure 20(b) (163 nm P-V), where the aspect ratio of tool path was optimized. For both the ring method and mesh method, the proposed tool path optimization achieved high accuracy in independently controlled FTS machining. Moreover, it was demonstrated that the proposed tool path optimization enabled to reduce form errors in advance and to achieve high accuracy in one-time cutting, which in turn contribute to the improvement of production efficiency.

It should be pointed out that in both two-dimensional sinewave and micro-lens array machining, the calculated form error from the machined surface profile was much larger than the predicted form error results. A possible reason is the influence of other error factors such as tool-related error and dynamic error in the diamond turning operation. Tool-related errors include tool contour error due to tool wear and tool

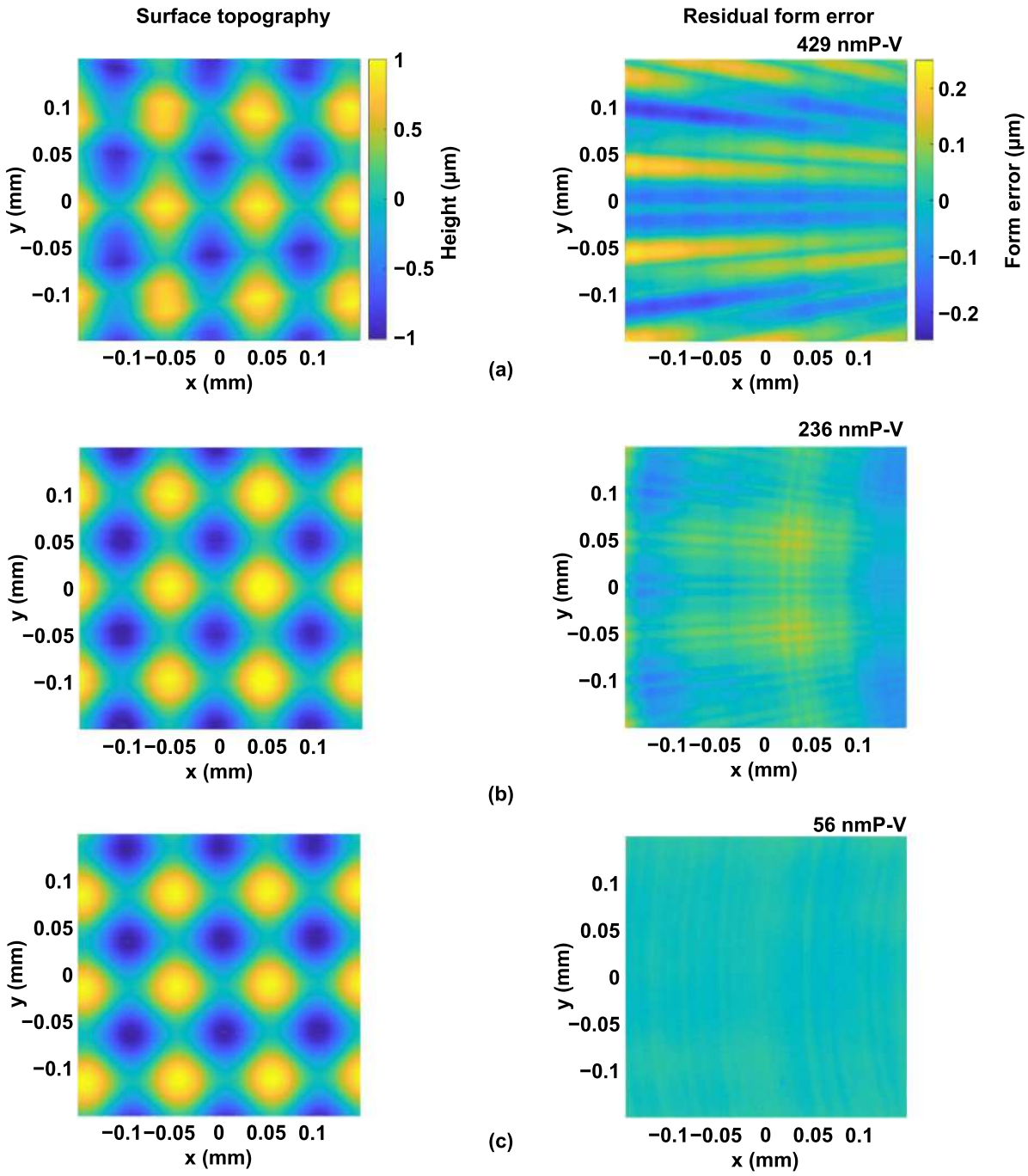

Figure 18. Micro topographies and residual form error distributions of the machined surface for (a) case 1, (b) case 2 and (c) case 3.

alignment error due to imperfect tool tip positioning [28]. These errors can be compensated by repositioning the tool and modifying the tool path [29, 30]. In addition, there is a dynamic error for FTS diamond turning especially tool path containing high frequency components. To compensate it, machining strategies such as adjusting compensating the tool path based on the inverse of dynamics model and splitting the machining into multiple operations have been mentioned [31–33]. Thus, in order to further improve the shape accuracy, it is necessary to focus on various error factors and compensation methods.

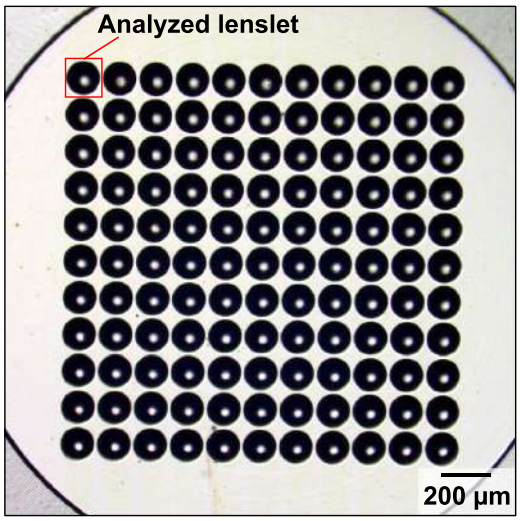

Figure 19. Microscope image of the machined micro-lens array.

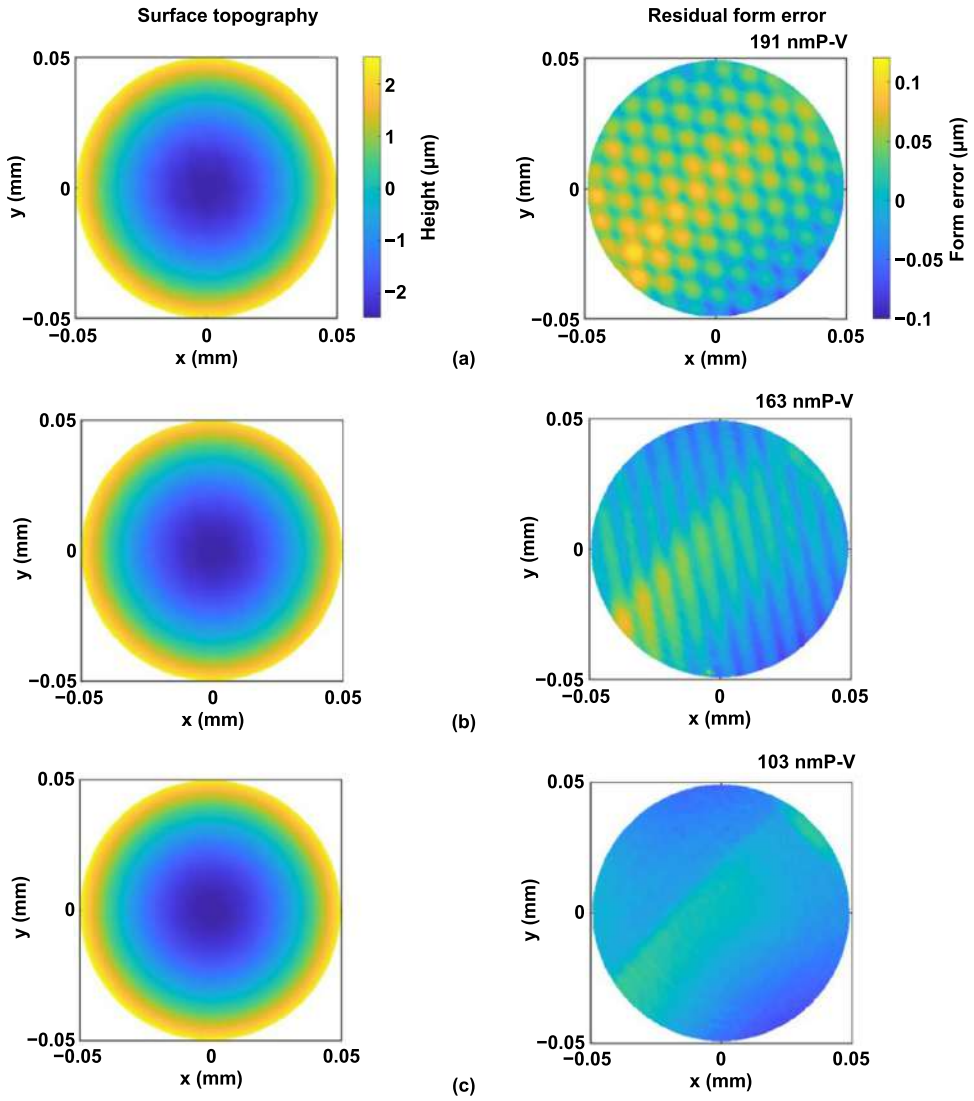

Figure 20. Micro topographies and residual form error distributions of the machined lenslet surface for (a) case 1, (b) case 2 and (c) case 3.

5. Conclusions

Tool path optimization method for an independently controlled FTS was established. The tool path program was generated using the ring method and mesh method instead of the conventional spiral tool path. The tool path was optimized by analyzing the effect of interpolation error using form error prediction. The optimization of control points layout consists of two steps. Initially, the number of control points is determined. Then, the optimal aspect ratio of the layout parameters is determined. Experimental validation by machining two-dimensional sinewaves and micro-lens arrays demonstrated the effectiveness of the tool path optimization method proposed in this study. The proposed method reduced the form error from 429 nm P-V to 56 nm P-V for two-dimensional sinewave with ring method, and from 191 nm P-V to 103 nm P-V for micro-lens arrays with mesh method, respectively.

This study establishes an important base for further developing ultraprecision machining technologies of freeform optics through diamond turning by using a FTS unit with a separate controller to achieve high accuracy without the necessity of trial and error, which contribute to advanced manufacturing of high value-added products.

Acknowledgments

This work has been supported by Japan Society for the Promotion of Science, Grant-in-Aid for Scientific Research (B), Project Number 21H01230. The authors would like to thank AMETEK Precitech Inc. for the technical supports of experimental equipment.

ORCID iD

Jiwang Yan https://orcid.org/0000-0002-5155-3604

References

[1] Fang F Z, Zhang X D and Hu X T 2008 Cylindrical coordinate machining of optical freeform surfaces *Opt. Express* **16** 7323–9
[2] Ye J F, Chen L, Li X H, Yuan Q and Gao Z S 2017 Review of optical freeform surface representation technique and its application *Opt. Eng.* **56** 110901
[3] Zhang Z Y, Yan J W and Kuriyagawa T 2019 Manufacturing technologies toward extreme precision *Int. J. Extreme Manuf.* **1** 022001
[4] Cheng D W, Wang Y T, Hua H and Talha M M 2009 Design of an optical see-through head-mounted display with a low f-number and large field of view using a freeform prism *Appl. Opt.* **48** 2655–68
[5] Jiang X, Scott P and Whitehouse D 2007 Freeform surface characterisation—a fresh strategy *CIRP Ann.* **56** 553–6
[6] De Chiffre L, Kunzmann H, Peggs G N and Lucca D A 2003 Surfaces in precision engineering, microengineering and nanotechnology *CIRP Ann.* **52** 561–77
[7] Mukaida M and Yan J W 2017 Ductile machining of single-crystal silicon for microlens arrays by ultraprecision diamond turning using a slow tool servo *Int. J. Mach. Tools Manuf.* **115** 2–14
[8] Weck M, Hennig J and Hilbing R 2001 Precision cutting processes for manufacturing of optical components *Proc. SPIE 4440, Lithographic and Micromachining Techniques for Optical Component Fabrication* (San Diego, CA: SPIE) pp 145–51
[9] Zhu W H, Jun M B and Altintas Y 2001 A fast tool servo design for precision turning of shafts on conventional CNC lathes *Int. J. Mach. Tools Manuf.* **41** 953–65
[10] Rakuff S and Cuttino J F 2009 Design and testing of a long-range, precision fast tool servo system for diamond turning *Precis. Eng.* **33** 18–25
[11] Kim H S, Kim E J and Song B S 2004 Diamond turning of large off-axis aspheric mirrors using a fast tool servo with on-machine measurement *J. Mater. Process. Technol.* **146** 349–55
[12] Kim H S and Kim E J 2003 Feed-forward control of fast tool servo for real-time correction of spindle error in diamond turning of flat surfaces *Int. J. Mach. Tools Manuf.* **43** 1177–83
[13] Precitech 2021 Fast tool servo (available at: www.precitech.com/product/accessoriesoverview/fasttoolservo (accessed 18 November 2021))
[14] To S, Kwok T C, Cheung C F and Lee W B 2005 Study of ultra-precision diamond turning of a microlens array with a fast tool servo system *Proc. SPIE* **6149** 61490S
[15] Yu D P, Gan S W, Wong Y S, Hong G S, Rahman M and Yao J 2012 Optimized tool path generation for fast tool servo diamond turning of micro-structured surfaces *Int. J. Adv. Manuf. Technol.* **63** 1137–52
[16] Zhu Z W and To S 2015 Adaptive tool servo diamond turning for enhancing machining efficiency and surface quality of freeform optics *Opt. Express* **23** 20234–48
[17] Dick L, Risse S and Tünnermann A 2021 Injection molded high precision freeform optics for high volume applications *Adv. Opt. Technol.* **1** 213–4
[18] Zhou M, Zhang H J and Chen S J 2010 Study on diamond cutting of nonrationally symmetric microstructured surfaces with fast tool servo *Mater. Manuf. Process.* **25** 488–94
[19] Neo D W K, Kumar A S and Rahman M 2014 A novel surface analytical model for cutting linearization error in fast tool/slow slide servo diamond turning *Precis. Eng.* **38** 849–60
[20] Gong H, Wang Y, Song L and Fang F Z 2015 Spiral tool path generation for diamond turning optical freeform surfaces of quasi-revolution *Comput. Aided Des.* **59** 15–22
[21] Scheiding S, Yi A Y, Gebhardt A, Li L, Risse S, Eberhardt R and Tünnermann A 2011 Freeform manufacturing of a microoptical lens array on a steep curved substrate by use of a voice coil fast tool servo *Opt. Express* **19** 23938–51
[22] Gao W, Araki T, Kiyono S, Okazaki Y and Yamanaka M 2003 Precision nano-fabrication and evaluation of a large area sinusoidal grid surface for a surface encoder *Precis. Eng.* **27** 289–98
[23] Kasztelanic R, Filipkowski A, Pysz D, Stepien R, Waddie A J, Taghizadeh M R and Buczynski R 2017 High resolution Shack–Hartmann sensor based on array of nanostructured GRIN lenses *Opt. Express* **25** 1680–91
[24] Oliveira O G, de Lima Monteiro D W and Costa R F O 2014 Optimized microlens-array geometry for Hartmann–Shack wavefront sensor *Opt. Lasers Eng.* **55** 155–61
[25] Press W H, Teukolsky S A, Vetterling W T and Flannery B P 1992 *Numerical Recipes in C : The Art of Scientific Computing* 2nd edn (Cambridge: Cambridge University Press) pp 123–4
[26] Li D, Qiao Z, Walton K, Liu Y T, Xue J D, Wang B and Jiang X Q 2018 Theoretical and experimental investigation of surface topography generation in slow tool servo ultra-precision machining of freeform surfaces *Materials* **11** 2566

[27] Yu D P, Wong Y S and Hong G S 2011 Optimal selection of machining parameters for fast tool servo diamond turning *Int. J. Adv. Manuf. Technol.* **57** 85–99
[28] Liu X L, Zhang X D, Fang F Z, Zeng Z, Gao H M and Hu X T 2015 Influence of machining errors on form errors of microlens arrays in ultra-precision turning *Int. J. Mach. Tools Manuf.* **96** 80–93
[29] Nagayama K and Yan J W 2020 Measurement and compensation of tool contour error using white light interferometry for ultra-precision diamond turning of freeform surfaces *Int. J. Autom. Technol.* **14** 654–64
[30] Nagayama K and Yan J W 2021 Deterministic error compensation for slow tool servo-driven diamond turning of freeform surface with nanometric form accuracy *J. Manuf. Process.* **64** 45–57
[31] Yu D P, Hong G S and Wong Y S 2011 Integral sliding mode control for fast tool servo diamond turning of micro-structured surfaces *Int. J. Autom. Technol.* **5** 4–10
[32] Yu D P, Hong G S and Wong Y S 2012 Profile error compensation in fast tool servo diamond turning of micro-structured surfaces *Int. J. Mach. Tools Manuf.* **52** 13–23
[33] Mukaida M and Yan J W 2017 Fabrication of hexagonal microlens arrays on single-crystal silicon using the tool-servo driven segment turning method *Micromachines* **8** 323